Reconstructing the southern South China Sea upper water column structure since the Last Glacial Maximum: Implications for the East Asian winter monsoon development

Stephan Steinke,[1,2] Mahyar Mohtadi,[1] Jeroen Groeneveld,[3] Li-Chuan Lin,[4] Ludvig Löwemark,[5] Min-Te Chen,[4] and Rebecca Rendle-Bühring[1]

Received 19 August 2009; revised 3 February 2010; accepted 19 February 2010; published 26 June 2010.

[1] Upper water column dynamics in the southern South China Sea were reconstructed in order to track changes in the activity of the East Asian winter monsoon (EAWM) since the Last Glacial Maximum. We used the difference in the stable oxygen isotopes ($\Delta\delta^{18}O$) and Mg/Ca-based temperatures (ΔT) of surface-dwelling (*G. ruber*) and thermocline-dwelling (*P. obliquiloculata*) planktonic foraminifera and the temperature difference between alkenone- and *P. obliquiloculata* Mg/Ca-based temperatures to estimate the upper ocean thermal gradient at International Marine Past Global Change Study (IMAGES) core MD01-2390. Estimates of the upper ocean thermal gradient were used to reconstruct mixed layer dynamics. We find that our $\Delta\delta^{18}O$ estimates are biased by changes in salinity and, thus, do not display a true upper ocean thermal gradient. The ΔT of *G. ruber* and *P. obliquiloculata* as well as the alkenone and *P. obliquiloculata* suggest increased surface water mixing during the late glacial, likely due to enhanced EAWM winds. Surface water mixing was weaker during the late Holocene, indicating a weaker influence of winter monsoon winds. The weakest winter monsoon activity occurred between 6.5 ka and 2.5 ka. Inferred EAWM changes since the Last Glacial Maximum coincide with EAWM changes as recorded in Chinese loess sediments. We find that the intensity of the EAWM and the East Asian summer monsoon show an inverse behavior during the last glacial and deglaciation but covaried during the middle to late Holocene.

Citation: Steinke, S., M. Mohtadi, J. Groeneveld, L.-C. Lin, L. Löwemark, M.-T. Chen, and R. Rendle-Bühring (2010), Reconstructing the southern South China Sea upper water column structure since the Last Glacial Maximum: Implications for the East Asian winter monsoon development, *Paleoceanography*, *25*, PA2219, doi:10.1029/2009PA001850.

1. Introduction

[2] The monsoon system represents one of the critical elements of global atmospheric circulation that controls the redistribution of latent and sensible heat. The seasonal reversal of the East Asian summer monsoon (EASM, May–August) and EAWM (October–March) dominates the winds, precipitation, the character of land vegetation and biota over SE Asia, and river runoff in the South China Sea (SCS). These seasonal changes in atmospheric circulation and precipitation affect the ocean leading to strong seasonality in current strength and direction, sea surface temperature (SST) and salinity (SSS), productivity, and upper water column structure of the SCS [*Wyrtki*, 1961].

[3] Changes in the East Asian monsoon (EAM) intensity have been previously reconstructed through the analysis of several proxy records (e.g., SST, SSS, and productivity) in marine sedimentary archives from the SCS [see *P. Wang et al.*, 2005, and references therein]. However, in the SCS, the interpretation of these proxy records in terms of EAM intensity variations is complicated because global ice volume induced eustatic sea level changes interact strongly with EAM variability [e.g., *Pelejero et al.*, 1999; *Tamburini et al.*, 2003; *Zhao et al.*, 2006, *Steinke et al.*, 2006; *Yu et al.*, 2006]. Reconstructed SSTs are a prominent example for the overriding control of sea level changes on SCS proxy records. Modern SST patterns in the SCS are controlled by the seasonal reversal of the summer and winter monsoon atmospheric circulation, whereas on glacial-interglacial time scales, SST patterns were strongly affected by sea level induced changes in the SCS basin geometry [e.g., *Pelejero et al.*, 1999; *Zhao et al.*, 2006].

[4] Salinity reconstructions are another example of the close interaction between EAM variability and sea level changes on SCS proxy records. In this context, salinity reconstructions are used to provide important information on the glacial-interglacial variability of the riverine runoff as a

[1]MARUM-Zentrum für Marine Umweltwissenschaften, University of Bremen, Bremen, Germany.
[2]State Key Laboratory of Marine Geology, Tongji University, Shanghai, China.
[3]Alfred-Wegener-Institut für Polar- und Meeresforschung, Bremerhaven, Germany.
[4]Institute of Applied Geosciences, National Taiwan Ocean University, Keelung, Taiwan.
[5]Department of Geology and Geochemistry, Stockholm University, Stockholm, Sweden.

0883-8305/10/2009PA001850

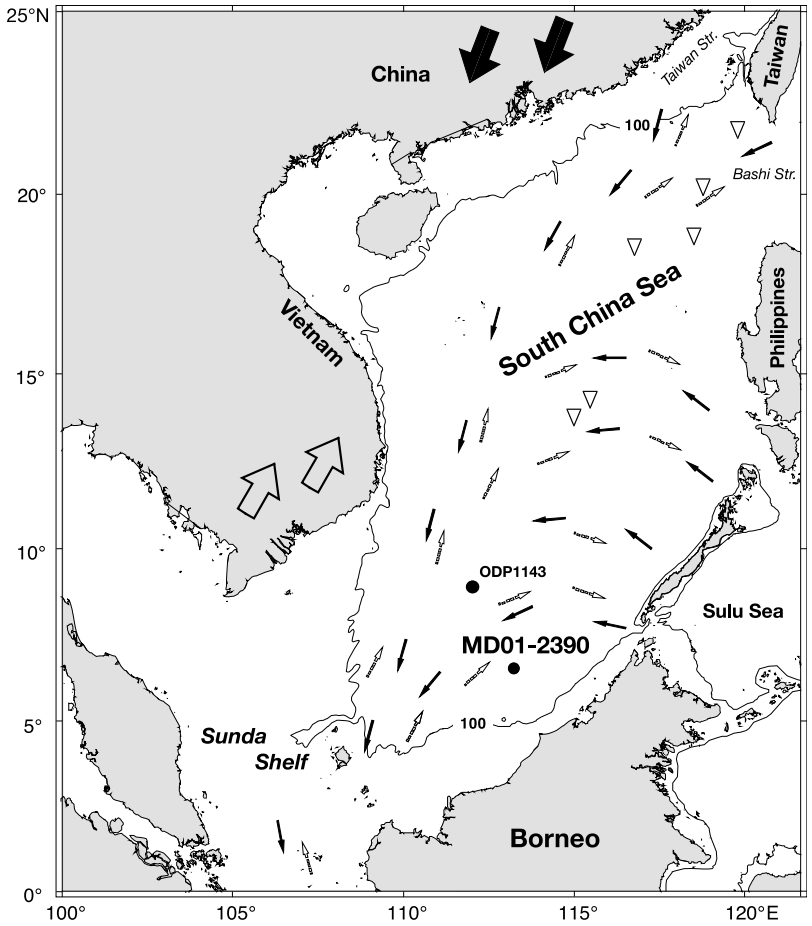

Figure 1. Map of the South China Sea showing the location of core MD01-2390. The location of core ODP Site 1143 [*Xu*, 2004; *Tian et al.*, 2005] and sediment traps (triangles [*Wiesner et al.*, 1996; *Tian et al.*, 2005; *Lin et al.*, 2004]) discussed in the text are also indicated. The 100 m isobath approximately represents the coastline during the Last Glacial Maximum (LGM). Small black arrows show the modern surface water circulation during northeasterly winter monsoon, and small open arrows show the surface water circulation during southwesterly summer monsoon. Modern surface water currents are adopted from *Wyrtki* [1961]. The large black and large open arrows indicate the wind direction during the winter monsoon and summer monsoon season, respectively.

result of changes in monsoon precipitation over the Asian continent, as demonstrated e.g., for the Bay of Bengal [*Kudrass et al.*, 2001] and the Andaman Sea [*Rashid et al.*, 2007]. Salinity reconstructions in the southern SCS, however, reflect the combined effects of sea level induced environmental changes (i.e., exposure of the Sunda shelf and closure of straits, phases of retreat and breakdown of the shelf drainage systems through flooding of the shelves) and EAM changes on glacial-interglacial time scales [*Steinke et al.*, 2006]. Therefore, they do not allow definite implications on the EAM intensity since the Last Glacial Maximum (LGM). Hence, the simple interpretation of EAM signals based on marine sediment proxy records in the SCS remains elusive [e.g., *P. Wang et al.*, 2005; *Yu et al.*, 2006]. Reliable marine proxies in the SCS that are unaffected by sea level variations are required in order to improve our understanding of the past behavior of the EAM.

[5] Because the upper part of the water column directly responds to seasonal changes in wind stress [*Wyrtki*, 1961; *Qu et al.*, 2007], reconstructing the state of the surface ocean structure represents a sensitive diagnostic variable of past changes in the EAM intensity. *Huang et al.* [1997] suggested that the EAWM winds strengthened in the northern SCS during the last glaciation, leading to a deep mixing of surface waters. Previous studies in the two prominent SCS upwelling areas off Vietnam and the Philippines suggested the alternating prevalence of winter and summer monsoons during glacial and interglacial intervals [*Jian et al.*, 2001; *Huang et al.*, 2003]. More recently, a long-term study (the last 1.5 Ma) using the oxygen isotope difference between subsurface (thermocline) dwelling and surface (mixed layer) dwelling planktonic foraminifera has revealed an increased mixed layer depth in the southern SCS during glacial periods, most likely due to stronger EAWM winds (ODP Site 1143 [*Tian et al.*, 2005]) (see Figure 1 for core location). In

contrast, a decreased mixed layer depth due to weaker winter monsoon winds characterizes the interglacial periods [*Tian et al.*, 2005; *Xu et al.*, 2005]. However, these studies used relatively long records in which temporal resolution is not sufficient to detect millennial-scale changes in the upper surface water structure. Consequently, the millennial-scale history of EAWM variability has not yet been fully determined in the southern SCS.

[6] Here we apply a multispecies approach of stable oxygen isotopes and Mg/Ca-based temperature differences between surface dwelling (two *G. ruber* white morphotypes; *G. ruber* sensu stricto (s.s.) and *G. ruber* sensu lato (s.l.)) and subsurface dwelling (*P. obliquiloculata*) planktonic foraminifera species from core MD01-2390 located in the southern SCS. In addition, we used the difference between alkenone- and *P. obliquiloculata* Mg/Ca-based temperatures. The aim of using the different approaches is to estimate the upper ocean thermal gradient and hence, past changes in surface ocean vertical structure since the LGM. Through the investigation of past changes in the surface ocean vertical structure, we are able to detect millennial-scale changes in the EAWM intensity in the southern tropical SCS region. Moreover, comparing multiproxy results from a single dated core allows us to determine potential biases of each specific approach.

2. Modern Oceanography and Hydrography

[7] Today, surface water masses and the hydrographic patterns of the SCS are largely controlled by the seasonally reversing EAM regime, which causes drift currents to change their flow direction [*Wyrtki*, 1961; *Shaw and Chao*, 1994] (Figure 1). During winter, high-pressure systems develop over Asia, causing cold and dry winds to persist (northeasterly monsoon), whereas in summer low pressure systems develop over Asia, drawing maritime tropical air masses in, and causing summer precipitation (southwesterly monsoon [*Ding*, 1994]). During the EAWM season, the dominant influence of the cold northeasterly winds together with the southward flow of the cold Chinese Coastal Waters result in low SSTs in the northern SCS and a strong north-south temperature gradient within the SCS. During the EASM season, warm Indian Ocean surface waters across the Sunda Shelf flow into the southern SCS [*Wyrtki*, 1961]. The resulting SSTs are uniformly high (~28°C–29°C) in the SCS. In the southern SCS, SST varies between ~27°C and ~29°C during the winter and summer seasons, respectively (Figure 2). Likewise, SSS in the SCS varies seasonally in response to the monsoonal rains. Annual changes in circulation pattern causes an interchange of low and high salinity surface water masses [*Wyrtki*, 1961]. The modern seasonal SSS in the southern SCS varies between 32.5 and 33.8 practical salinity units (World Ocean Atlas 2005 [*Locarnini et al.*, 2006]) with the minimum SSS typically occurring during winter (October to January), when winter monsoon precipitation prevails. The combination of high pressure over Asia and low pressure over Australia pushes the Inter Tropical Convergence Zone (ITCZ) southward, resulting in e.g., highest rainfall over Borneo and consequently a maximum in river runoff [*Stephens et al.*, 2008]. The opposite is true during the summer when the ITCZ migrates further north.

[8] Surface ocean structure (the depth of thermocline and the mixed layer) is also controlled by the annual reversal of the EAM winds. The mixed layer depth in the SCS varies between 30 m to 40 m during the summer monsoon, and 70 m to 80 m during the winter monsoon season (Figure 3) [*Wyrtki*, 1961; *Qu et al.*, 2007]. Thermocline is deepest in the northern SCS during winter and shoals southward. Annual variations in the depth of the mixed layer are weaker in the southern SCS compared to the northern SCS [*Qu et al.*, 2007]: the mixed layer is shallowest in April–May (<35 m) and approaches its seasonal maximum in August–October (>55 m [*Qu et al.*, 2007]). The deepening of the mixed layer in the southern SCS is most likely due to wind stirring and downward Ekman pumping forced by the southwest summer monsoon [*Qu et al.*, 2007].

3. Strategy and Proxy Variables Used for Reconstructing the Southern SCS Upper Water Column Structure

[9] The oxygen isotope difference ($\Delta\delta^{18}O$) between surface- and subsurface-dwelling planktonic foraminifera species is a common method used for reconstructing the upper water column structure, and a qualitative estimate for the state of the upper ocean thermal gradient over a certain time period [e.g., *Ravelo and Fairbanks*, 1992; *Ravelo and Shackleton*, 1995; *Ravelo and Andreasen*, 1999]. The $\Delta\delta^{18}O$ between shallow-dwelling species and subsurface-dwelling species is usually large when the thermocline is shallow and a large temperature range exists within the photic zone. In contrast, small isotopic differences normally indicate a deepened thermocline with a narrow temperature range within the photic zone [*Ravelo and Shackleton*, 1995; *Ravelo and Andreasen*, 1999]. An underlying assumption of this approach is that the planktonic foraminifera have the same seasonal occurrence and a relative stable depth habitat throughout their ontogenetic cycle. Therefore, their stable isotopic compositions should reflect differences in the physical and chemical properties between surface and subsurface water masses. Another assumption is that species variations and bioturbation only play a minor role in controlling the distribution of different species and their isotopic values [cf. *Löwemark et al.*, 2008].

[10] *Tian et al.* [2005] used the $\Delta\delta^{18}O$ of mixed layer dwelling species *G. ruber* and thermocline dwelling species *P. obliquiloculata* to infer long-term changes in the upper ocean thermal gradient and hence, the EAWM intensity in the southern SCS. *G. ruber* has been found to live and calcify predominantly in the upper 60 m of the mixed layer/water column [*Fairbanks et al.*, 1980, 1982; *Hemleben et al.*, 1989]. Sediment trap data from the SCS show a more or less year-round occurrence of *G. ruber* [*Wiesner et al.*, 1996; *Lin et al.*, 2004; *Tian et al.*, 2005]. In contrast, *P. obliquiloculata* has a preferred depth habitat at the uppermost thermocline [*Ravelo and Fairbanks*, 1992; *Cléroux et al.*, 2007; *Farmer et al.*, 2007; *Mohtadi et al.*, 2009]. Based on sediment trap deployments, *P. obliquiloculata* reveals highest fluxes during the winter monsoon season (December

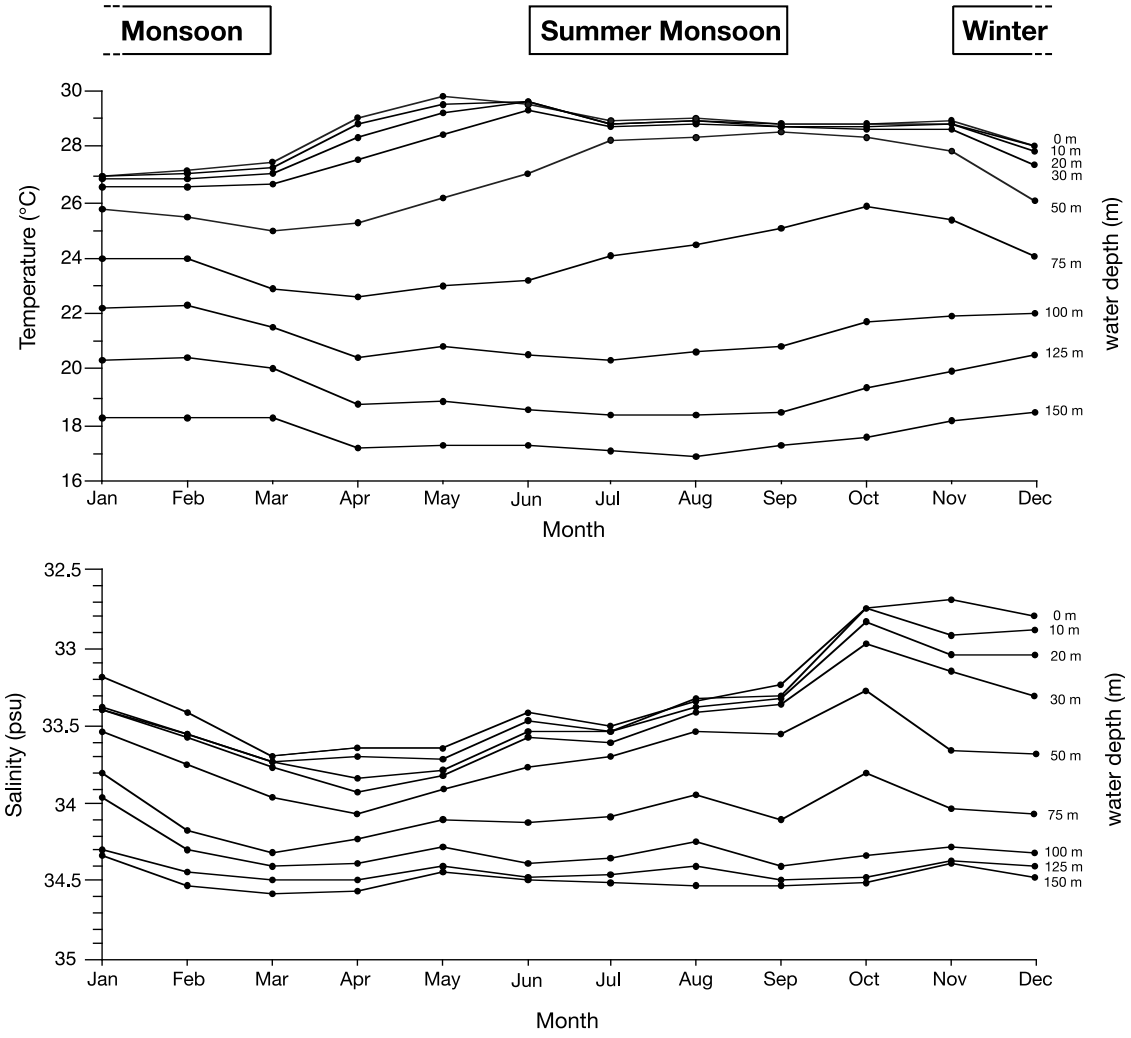

Figure 2. Monthly (top) temperature and (bottom) salinity for the upper 150 m of the water column in the southern South China Sea at 112.5°E and 6.5°N (World Ocean Atlas 2005 data [*Locarnini et al.*, 2006; *Antonov et al.*, 2006]).

to March) in the SCS [*Tian et al.*, 2005; *Lin and Hsieh*, 2007]. *Tian et al.* [2005] demonstrated that oxygen isotope measurements of core top samples from the SCS reveal larger $\Delta\delta^{18}$O between *P. obliquiloculata* and *G. ruber* in the SCS upwelling areas with a shallow thermocline. In contrast, $\Delta\delta^{18}$O is smaller in nonupwelling areas with a deeper thermocline [*Tian et al.*, 2005]. This indicates the great potential of this approach for reconstructing the upper water column structure in the SCS, whereby the $\Delta\delta^{18}$O is thought to represent the temperature difference between the surface and the thermocline waters.

[11] Unlike to the study of *Tian et al.* [2005], we used two morphotypes of *G. ruber* in order to test the effect of the different *G. ruber* morphotypes on the upper ocean thermal gradient estimates. According to *Wang* [2000], the two morphotypes of *G. ruber* (white; *G. ruber* s.s. and *G. ruber* s.l.) inhabit different depths. *G. ruber* s.s. predominantly inhabits the upper ~30 m of the surface waters whereas *G. ruber* s.l. is suggested to live below 30 m and/or the surface salinity layer in the modern SCS [*Wang*, 2000]. This is supported by studies from the subtropical gyre in the North Pacific [*Kawahata*, 2005] and the seas around Japan [*Kuroyanagi and Kawahata*, 2004], which suggest that *G. ruber* s.s. is predominant in the surface waters while *G. ruber* s.l. is predominant in deeper waters. These findings are also supported by Mg/Ca ratios and stable isotopes, indicating a colder calcite precipitation temperature for *G. ruber* s.l. shells compared to *G. ruber* s.s. [*Löwemark et al.*, 2005; *Steinke et al.*, 2005]. This suggests that *G. ruber* s.l. calcifies at a greater depth in the surface waters than *G. ruber* s.s. [*Löwemark et al.*, 2005; *Steinke et al.*, 2005].

[12] We further analyzed the δ^{18}O of another planktonic foraminifera species *N. dutertrei* in order to test the reliability of *P. obliquiloculata* in representing conditions at the bottom of the mixed layer or the uppermost thermocline. *N. dutertrei* is a subsurface dweller that usually reaches its maximum abundance at the thermocline [*Fairbanks et al.*, 1982; *Curry et al.*, 1983].

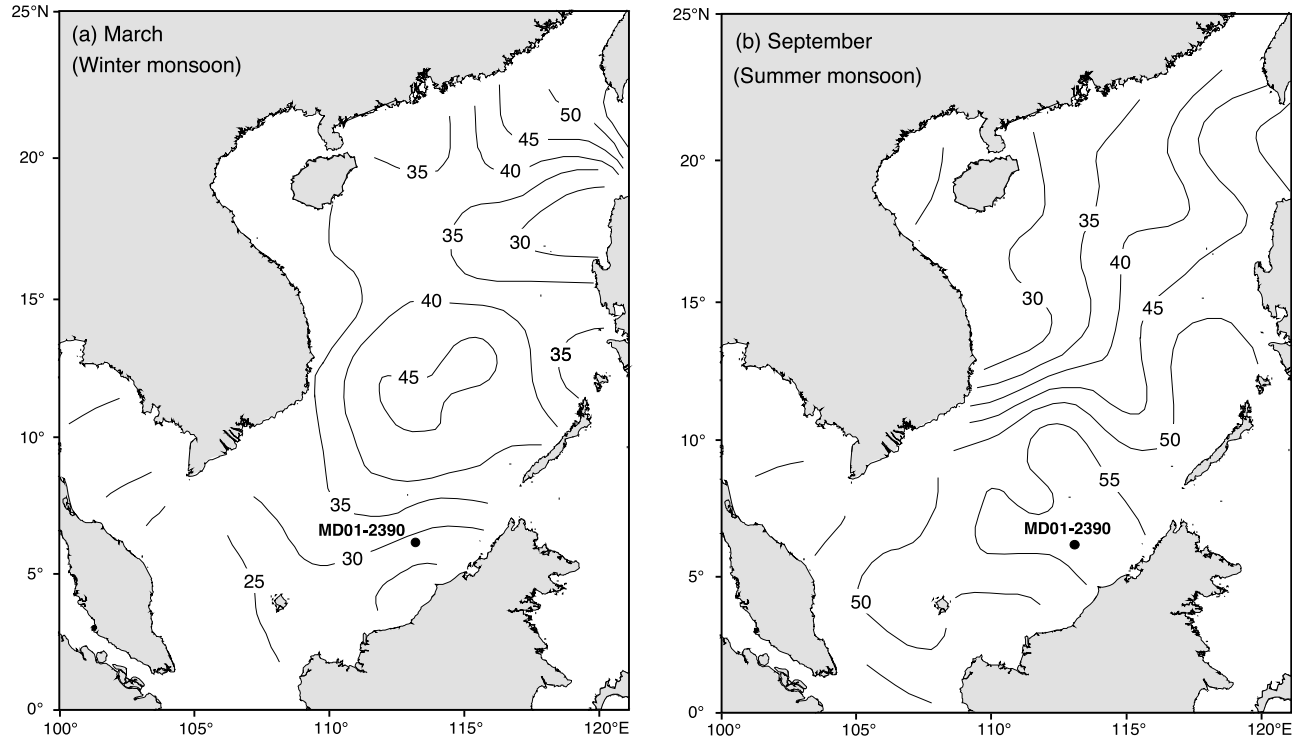

Figure 3. Isothermal depth (proxy for mixed layer depth (MLD)) redrawn from *Qu et al.* [2007] during March and September in the South China Sea. The isothermal depth in the southern South China Sea is shallowest during March–May (<35 m) and approaches its seasonal maximum in August–October (>55 m [*Qu et al.*, 2007]). Note the seasonal reversal of the gradient in mixed layer depth between the southern and northern South China Sea.

[13] In addition to the approach of *Tian et al.* [2005], we estimated the relative depth of the mixed layer using two other approaches. The first is the Mg/Ca-based temperature difference between the two *G. ruber* morphotypes and *P. obliquiloculata* ($\Delta T_{(G.\ ruber\text{-}P.\ obliquiloculata)}$). The second approach uses the difference in alkenone- and *P. obliquiloculata* Mg/Ca-based temperatures to infer changes in the upper ocean thermal gradient in the southern SCS since the LGM. With respect to the seasonal occurrence of alkenone-producing coccolithophores, a sediment trap study together with water sample collections from the northern SCS showed that the alkenone-producing coccolithophores *Emiliania huxleyi* and *Gephyrocapsa oceanica* predominantly occur in the cold months (winter and spring), when the northeastern monsoon prevails [*Wiesner et al.*, 1996; *Chen et al.*, 2007].

4. Material and Methods

[14] Samples were taken from CALYPSO gravity core MD01-2390 (06.38, 12°N; 113.24, 56°E; water depth of 1545 m) that was recovered on the Nansha Shallow of the southern SCS during R/V *Marion Dufresne* 122/IMAGES VII-WEPAMA [*Steinke et al.*, 2006] (Figure 1). Previous analyses for core MD01-2390 have included *G. ruber* morphotype-specific $\delta^{18}O$ and Mg/Ca analyses [*Steinke et al.*, 2006, 2008] and alkenone determinations for the depth interval 350–900 cm (11–19 ka [*Steinke et al.*, 2006, 2008]). In this study, the original chronological framework published by *Steinke et al.* [2006, 2008] has been improved by three additional AMS-^{14}C ages (Table 1; see below).

4.1. Radiocarbon Dating

[15] Additional accelerator mass spectrometry (AMS) ^{14}C datings were performed on monospecific samples of planktonic foraminifera *Globigerinoides sacculifer*. Radiocarbon age determinations were performed at the National Ocean Sciences Accelerator Mass Spectrometry Facility, Woods Hole, USA. Conventional radiocarbon ages were corrected for isotopic fractionation using $\delta^{13}C$ values. All radiocarbon ages were calibrated using CALIB 5.0.1 radiocarbon software [*Stuiver et al.*, 1998] and the marine 04.14c data set [*Hughen et al.*, 2004] without adjusting for a regional ^{14}C reservoir age (ΔR = deviation from the average global reservoir age of ~400 years; Table 1). Ages have been linearly interpolated between age control points using the program AnalySeries 1.1 [*Paillard et al.*, 1996]. In the following, all ages refer to calibrated (cal) years B.P.

4.2. Stable Oxygen Isotopes

[16] Core MD01-2390 was sampled at 5 cm intervals (12.5–597.5 cm) and 10 cm intervals (602.5–907.5 cm) for

Table 1. AMS-^{14}C Ages and Calendar Ages of Core MD01-2390

Laboratory Code	Sample Depth (cm)	Foraminifera Species	^{14}C age (years B.P.)	Calendar Age B.P.[a]	1σ Calendar Age Range[b]
NUTA2-7997[c]	12.5	*G. sacculifer*	1505 ± 35	1050	998–1109 (1.0)
NOSAMS-OS-64773[d]	62.5	*G. sacculifer*	2880 ± 30	2620; 2680	2611–2630 (0.13); 2644–2718 (0.87)
NUTA2-7998[c]	92.5	*G. sacculifer*	3550 ± 35	3430	3378–3475 (1.0)
NOSAMS-OS-64821[d]	152.5	*G. sacculifer*	4850 ± 35	5090; 5180	5079–5099 (0.12); 5110–5243 (0.88)
NOSAMS-OS-64774[d]	227.5	*G. sacculifer*	7660 ± 35	8110	8063–8166 (1.0)
NUTA2-7999[c]	317.5	*G. sacculifer*	9860 ± 45	10,720; 10,870	10,624–10,812 (0.92); 10,854–10,878 (0,07)
NUTA2-8036[c]	557.5	*G. sacculifer* + *G. ruber*	14,080 ± 55	16,270	16,077–16,468 (1.0)

[a]The ^{14}C ages were calibrated using CALIB 5.0.1 and the marine 04.14c data set [*Hughen et al.*, 2004] without a further adjustment for a regional ^{14}C reservoir age (ΔR = deviation from the average global reservoir age of 400 years).
[b]Here 1σ enclosing 68.3% of probability distribution [*Stuiver et al.*, 1998]. Values in parentheses are the relative area under probability distribution.
[c]Measured at the Nagoya University Center for Chronological Research, Japan. Published previously by *Steinke et al.* [2006].
[d]Measured at the National Ocean Sciences Accelerator Mass Spectrometry Facility, Woods Hole, USA. This study.

δ^{18}O analyses on *P. obliquiloculata* yielding a sample resolution of ~140–200 years. *N. dutertrei* was picked in 10 cm intervals, equivalent to a sample resolution of ~200 years. The sample preparation followed standard procedures: the dried bulk samples were washed over a 63 μm sieve, dried at 40°C in an oven, and subsequently dry sieved into subfractions. Oxygen isotope ratios were determined on samples composed of 15–20 specimens of *P. obliquiloculata* in the 250–350 μm size fraction. About 15–20 specimens of *N. dutertrei* were picked from the 355–400 μm size fraction. *P. obliquiloculata* samples were analyzed using a Finnigan MAT 251 mass spectrometer with an automated carbonate preparation device at the Leibniz Laboratory (University of Kiel). *N. dutertrei* samples were analyzed at the Department of Geosciences (University of Bremen). The standard error of the δ^{18}O analyses in Kiel and Bremen is < 0.08‰.

4.3. Mg/Ca Paleothermometry

[17] Mg/Ca analyses of *P. obliquiloculata* were performed on a subset of samples with 5 to 40 cm spacing (~150–300 year per sample). For each sample, approximately 30–40 specimens of *P. obliquiloculata* were picked out of the 250–350 μm size fraction. Foraminiferal tests were cleaned in successive steps following the cleaning protocol developed by *Barker et al.* [2003] and analyzed with a Perkin Elmer Optima 3300R ICP-OES at the Department of Geosciences, University of Bremen. Analytical precision for Mg/Ca ratios is 0.095%. The reproducibility of the ICP-OES technique, tested by replicate measurements, is 0.11 mmol/mol. The Mg/Ca ratios are not affected either by the occurrence of synsedimentary and postdepositional precipitated Mn oxide and Mn-rich carbonate coatings, or by postdepositional partial dissolution [*Steinke et al.*, 2006, 2008]. Thermocline water temperature based on *P. obliquiloculata* was calculated using the species-specific calibration equation by *Anand et al.* [2003]:

$$\mathrm{Mg/Ca\ (mmol/mol)} = 0.328\ \exp[0.090\ \mathrm{SST}\ (^{\circ}\mathrm{C})]$$

The standard error of estimates for various temperature equations derived from core top and trap calibrations is typically in the range of 0.5°C-1.0°C [*Lea et al.*, 2000; *Elderfield and Ganssen*, 2000; *Anand et al.*, 2003].

4.4. Alkenone Paleothermometry

[18] Alkenone analyses of the upper 350 cm of the core were performed on ~1.5 g freeze-dried and homogenized sediments. Alkenones were extracted by ultrasonication using a sequence of two solvents: dichloromethane and methanol. An aliquot of the lipid extract was separated into four fractions (F1, 3 ml of hexane; F2, 3 ml of hexane:toluene (3:1); F3, 4 ml of toluene; F4, 3 ml of toluene:methanol (3:1)) by silica gel column chromatography (SiO_2 with 5% distilled water; ID, 5.5 mm; length, 45 mm). n-$C_{24}D_{50}$ and n-$C_{36}H_{74}$ were added as internal standards into the F1 (n-alkenes) and F3 (alkenones and alkenoates) fractions, respectively. Gas chromatography was conducted using a Hewlett Packard 5890 series N gas chromatograph (GC) with cool on-column injection and electron pressure control systems and a flame ionization detector (FID) at the National Taiwan Ocean University, Keelung. Samples were dissolved in hexane. Helium was used as a carrier gas, and the flow velocity was maintained at 30 cm/s. For the analyses of the F3 (alkenones and alkenoates) fraction, the oven temperature was programmed from 70°C to 290°C at 20°C/min, 290°C to 310°C at 0.5°C/min., and then isothermal at 310°C for more than 30 min.

[19] Given the seasonal preference of alkenone-producing coccolithophores for the winter season [*Chen et al.*, 2007] (see also discussion by *Steinke et al.* [2008]), SSTs were calculated using the equation developed by *Pelejero and Grimalt* [1997]. This was established by correlating the $U^{K'}_{37}$ index in core top sediments from the SCS with winter water column temperatures for the top 30 m:

$$U^{K'}_{37} = 0.014 \pm 0.002\ \mathrm{SST}\ (^{\circ}\mathrm{C}) + 0.573 \pm 0.052$$

Since this equation gives unreliable high temperature estimates for the late Holocene in the order of 29.8°C, which are even higher than modern summer SSTs (see Figure 2), the linear regression equation has been modified by using a slope of 0.015. The latter yields late Holocene winter SST estimates that are in relatively good agreement with modern winter SSTs in the study area, and is statistically justified by the fact that the slope of 0.015 lies within the standard error (±0.002) of the linear regression equation developed by *Pelejero and Grimalt* [1997]. The mean standard error of

estimated temperatures for various temperature equations is around 1°C [e.g., *Conte et al.*, 2006]. Alkenone determinations for the depth interval 350–750 cm were previously published by *Steinke et al.* [2008].

4.5. Seawater $\delta^{18}O$ Estimates

[20] $\delta^{18}O_{seawater}$ (= proxy for sea surface water salinity) was calculated by removing the temperature component from the *G. ruber* morphotype-specific $\delta^{18}O$ records using the temperature-$\delta^{18}O_{seawater}$ relationship given by *Bemis et al.* [1998]:

$$\delta^{18}O_{seawater} = (T - 16.5 + 4.8^{*}\ \delta^{18}O_{calcite})/4.8 + 0.27$$

where $\delta^{18}O_{calcite}$ is the measured $\delta^{18}O$ of the two *G. ruber* morphotypes, and T the *G. ruber* morphotype-specific Mg/Ca-based temperatures. The component of $\delta^{18}O_{seawater}$ that is attributed to changes in the local/regional hydrology was then calculated by subtracting the effect of continental ice volume using the *Waelbroeck et al.* [2002] corrections.

5. Results

5.1. Age Model

[21] The original age model of core MD01-2390 is based on AMS-^{14}C dating and is corroborated by comparing the *G. ruber* s.s. $\delta^{18}O$ record to previously published ^{14}C-dated oxygen isotope records of the SCS [*Wang et al.*, 1999; *Pelejero et al.*, 1999; *Kienast et al.*, 2001; *Steinke et al.*, 2001; *Chen et al.*, 2005]. The new age model has been improved by three additional ages for the Holocene (Table 1). The original age model and the *G. ruber* s.s. $\delta^{18}O$ record have been discussed and published previously by *Steinke et al.* [2006, 2008] (Table 1).

5.2. Stable Oxygen Isotopes and $\Delta\delta^{18}O_{(thermocline\text{-}mixed\ layer\ dweller)}$

[22] Time series of $\delta^{18}O$ for *G. ruber* s.s., *G. ruber* s.l. [*Steinke et al.*, 2008], *P. obliquiloculata*, and *N. dutertrei* (this study), cover the past ~21 ka (Figure 4a). Our $\delta^{18}O$ values suggest that the habitat of *P. obliquiloculata* partially overlap with that of *N. dutertrei* (Figure 4a). The $\Delta\delta^{18}O_{(P.\ obliquiloculata\ -\ G.\ ruber\ s.s.)}$, $\Delta\delta^{18}O_{(P.\ obliquiloculata\ -\ G.\ ruber\ s.l.)}$, $\Delta\delta^{18}O_{(N.\ dutertrei\ -\ G.\ ruber\ s.s.)}$, and $\Delta\delta^{18}O_{(N.\ dutertrei\ -\ G.\ ruber\ s.l.)}$ are shown in Figures 4b and 4c. The $\Delta\delta^{18}O_{(P.\ obliquiloculata\ -\ G.\ ruber\ s.s.)}$ estimates reveal slightly higher values (~1.8‰) during the last glacial compared to the late Holocene (~1.5‰; Figure 4b), whereas the $\Delta\delta^{18}O_{(P.\ obliquiloculata\ -\ G.\ ruber\ s.l.)}$ estimates yield more or less comparable values during these two periods. The $\Delta\delta^{18}O_{(P.\ obliquiloculata\ -\ G.\ ruber\ s.s.)}$, and $\Delta\delta^{18}O_{(P.\ obliquiloculata\ -\ G.\ ruber\ s.l.)}$ records are offset by ~0.1‰ to 1.3‰ over the investigated period, and most pronounced between 15 and 8 ka (Figure 4b). The period between 18 and 15 ka is characterized by two short-lasting episodes of decreased $\Delta\delta^{18}O$ (Figure 4b). The second low in $\Delta\delta^{18}O$ around 15.5 ka is even more pronounced in $\Delta\delta^{18}O_{(P.\ obliquiloculata\ -\ G.\ ruber\ s.l.)}$. Starting at ~15 ka, the $\Delta\delta^{18}O_{(P.\ obliquiloculata\ -\ G.\ ruber)}$ values increase, but this increasing trend is punctuated by lower values around the Younger Dryas (YD) period, and largest differences are reached between 11.3 ka and 7.5 ka. Thereafter, the $\Delta\delta^{18}O_{(P.\ obliquiloculata\ -\ G.\ ruber)}$ values gradually decrease. Both $\Delta\delta^{18}O_{(N.\ dutertrei\ -\ G.\ ruber)}$ downcore records generally parallel the $\Delta\delta^{18}O_{(P.\ obliquiloculata\ -\ G.\ ruber)}$ records, except for 16–15 ka (Figure 4c). Slightly increased $\Delta\delta^{18}O_{(N.\ dutertrei\ -\ G.\ ruber)}$ values during the LGM are followed by a period of lower differences around 18–15 ka. $\Delta\delta^{18}O_{(N.\ dutertrei\ -\ G.\ ruber)}$ values increased again between 11 to 8 ka. After 8 ka, $\Delta\delta^{18}O_{(N.\ dutertrei\ -\ G.\ ruber)}$ values progressively decreased to the late Holocene values of ~1.3‰ (Figure 4c).

5.3. Mg/Ca Paleothermometry and $\Delta T_{(G.\ ruber\text{-}P.\ obliquiloculata)}$

[23] Mg/Ca-based thermocline temperatures using *P. obliquiloculata* suggest similar temperatures for the LGM and late Holocene periods ranging between ~20°C and 22°C. Lower thermocline temperatures occurred between 17.5 and 15.5 ka (~16°C to 20°C) and 5–3 ka (~18°C to 20°C; Figure 5b). Mg/Ca-based SST reconstructions on the two *G. ruber* morphotypes have been shown to range from 24.8°C to 28.8°C, and 23.5°C to 27.6°C during the last ~21 ka [*Steinke et al.*, 2006, 2008]. ΔT reconstructions using both *G. ruber* morphotypes reveal a smaller (~4°C) thermal gradient between surface and subsurface waters during the last glacial compared to the late Holocene. $\Delta T_{(G.\ ruber\ -\ P.\ obliquiloculata)}$ shows an overall increase during the last deglaciation and early Holocene (Figure 5). Largest ΔT between the surface and thermocline waters occurred between 6.5 ka and 2.5 ka (Figure 5c).

5.4. Alkenone Paleothermometry and $\Delta T_{(Alkenones\text{-}P.\ obliquiloculata)}$

[24] The alkenone-derived SST estimates reveal late glacial "wintertime" temperatures around 23.5°C (17–19 ka; Figure 5a). Lowest temperatures of 22°C–23°C are recorded between 15 and 17 ka, almost coeval with the North Atlantic Heinrich Event 1 [*Steinke et al.*, 2008]. Holocene temperature estimates range between 24.6°C and 27.8°C (Figure 5a). The $\Delta T_{(Alkenones\ -\ P.\ obliquiloculata)}$ reconstruction reveals a smaller (~0.5°C–4°C) thermal gradient between surface and subsurface waters during the last glacial compared to the late Holocene (Figure 5d). After ~15 ka, the $\Delta T_{(Alkenones\ -\ P.\ obliquiloculata)}$ shows an overall increase until ~4.5 ka (Figure 5c). Like the $\Delta T_{(G.\ ruber\ -\ P.\ obliquiloculata)}$, the $\Delta T_{(Alkenones\ -\ P.\ obliquiloculata)}$ estimates reveal largest values around 4.5 ka (Figure 5d).

5.5. Seawater $\delta^{18}O$ Variations

[25] The inferred $\delta^{18}O_{seawater}$ records using *G. ruber* s.s. (*G. ruber* s.l.) $\delta^{18}O$ and Mg/Ca-based estimates reveal average $\delta^{18}O_{seawater}$ values of approximately −0.94‰ (−0.73 ‰) during the LGM and values of −0.55‰ (−0.37‰) during the late Holocene (0–5 ka; Figure 4d). Our $\delta^{18}O_{seawater}$ values suggest a decrease in local salinity during the LGM compared to the late Holocene. Lower $\delta^{18}O_{seawater}$ values compared to late Holocene values occurred during the Bølling-Allerød (B/A) and the early Holocene around 11−8 ka. Increased $\delta^{18}O_{seawater}$ values occurred between

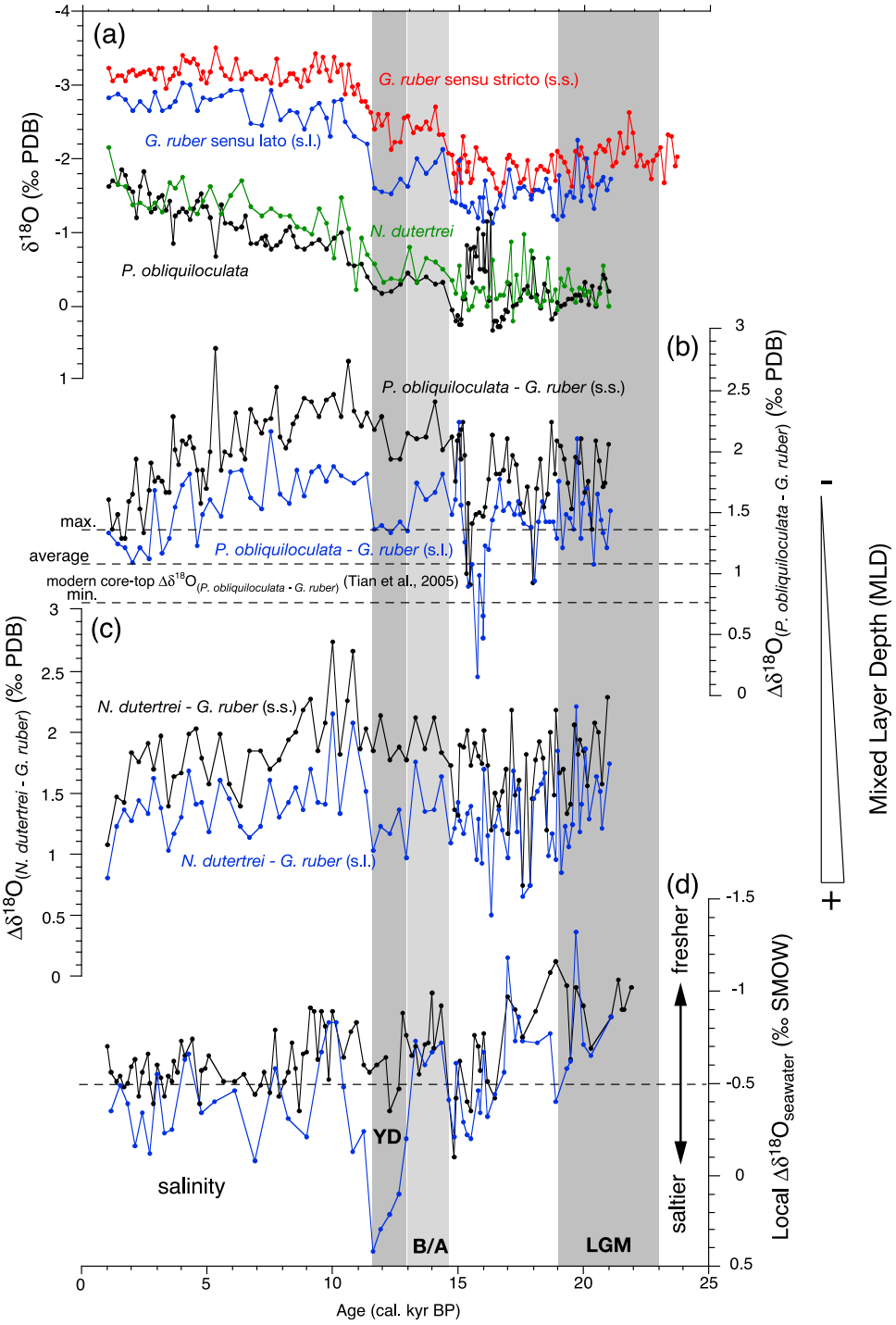

Figure 4. Proxy records of the upper water column structure and inferred paleo-$\delta^{18}O_{seawater}$ record at core site MD01-2390 since the LGM: (a) oxygen isotope records of *G. ruber* s.s. [*Steinke et al.*, 2008], *G. ruber* s.l. [*Steinke et al.*, 2008], *N. dutertrei* (this study), and *P. obliquiloculata* (this study); (b) $\Delta\delta^{18}O_{(P.\ obliquiloculata\ -\ G.\ ruber\ s.s.)}$ (black) and $\Delta\delta^{18}O_{(P.\ obliquiloculata\ -\ G.\ ruber\ s.l.)}$ (blue); (c) $\Delta\delta^{18}O_{(N.\ dutertrei\ -\ G.\ ruber\ s.s.)}$ (black) and $\Delta\delta^{18}O_{(N.\ dutertrei\ -\ G.\ ruber\ s.l.)}$ (blue); and (d) $\delta^{18}O_{seawater}$ records using both the stable oxygen isotopes and Mg/Ca-SST estimates derived from *G. ruber* s.s. (black) and *G. ruber* s.l. (blue). Shaded bars indicate the Younger Dryas (YD) (age adopted from *Stuiver et al.* [1995]), Bølling-Allerød (B/A) (age adopted from *Stuiver et al.* [1995]), and Last Glacial Maximum (LGM) (19,000–23,000 cal years B.P.; EPILOG chronozone [*Mix et al.*, 2001]).

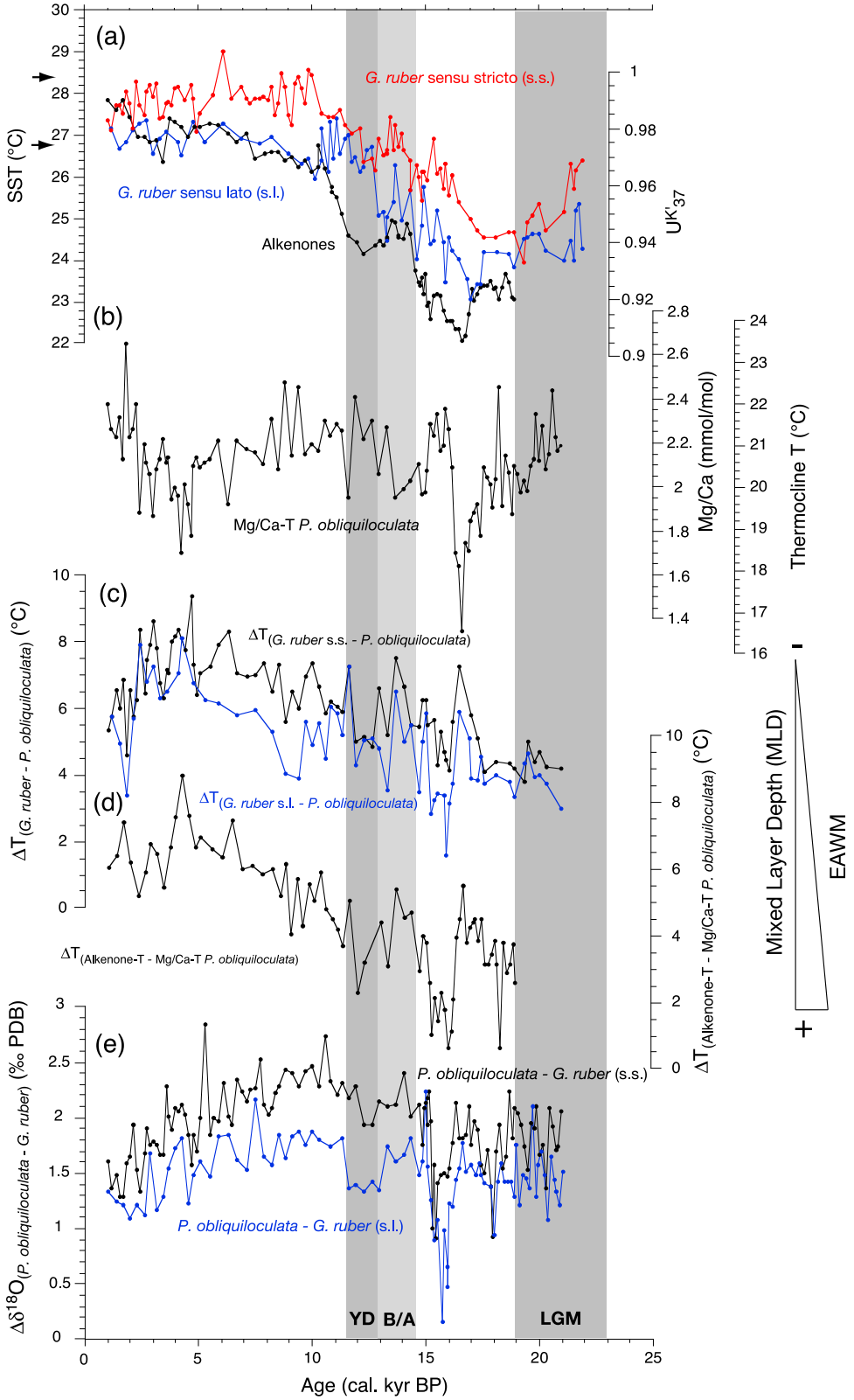
(a)
G. ruber sensu stricto (s.s.)
G. ruber sensu lato (s.l.)
Alkenones
SST (°C)
UK'37
(b)
Mg/Ca-T P. obliquiloculata
Mg/Ca (mmol/mol)
Thermocline T (°C)
(c)
ΔT(G. ruber s.s. - P. obliquiloculata)
(d)
ΔT(G. ruber s.l. - P. obliquiloculata)
ΔT(Alkenone-T - Mg/Ca-T P. obliquiloculata)
ΔT(G. ruber - P. obliquiloculata) (°C)
ΔT(Alkenone-T - Mg/Ca-T P. obliquiloculata) (°C)
(e)
P. obliquiloculata - G. ruber (s.s.)
P. obliquiloculata - G. ruber (s.l.)
Δδ18O(P. obliquiloculata - G. ruber) (‰ PDB)
YD
B/A
LGM
Mixed Layer Depth (MLD)
EAWM
Age (cal. kyr BP)

Figure 5

17 and 15 ka and during the YD period (Figure 4d), indicating higher salinities during these periods.

6. Discussion

6.1. Comparison of Different Proxy Records

[26] Results from this study yield a more complex picture of upper ocean thermal gradient variations in the southern SCS compared to previous studies [*Xu*, 2004; *Tian et al.*, 2005]. More importantly, the different proxy approaches based on planktonic foraminiferal $\delta^{18}O$, Mg/Ca-based and alkenone-based temperature estimates reveal significant differences.

[27] 1. The $\Delta\delta^{18}O$ records yield slightly higher $\Delta\delta^{18}O$ values ($\Delta\delta^{18}O_{(P.\ obliquiloculata\ -\ G.\ ruber\ \text{s.s.})}$; Figure 4b) or similar values ($\Delta\delta^{18}O_{(P.\ obliquiloculata\ -\ G.\ ruber\ \text{s.l.})}$; Figure 4b) for the LGM compared to late Holocene. Core top data of *Tian et al.* [2005] range from 0.76‰ to 1.38‰, with an average value of 1.09‰ for the southern SCS (see Figure 4b). Hence, the $\Delta\delta^{18}O_{(P.\ obliquiloculata\ -\ G.\ ruber\ \text{s.s.})}$ estimates suggest weaker mixing in the southern SCS during the LGM compared to the late Holocene, whereas the $\Delta\delta^{18}O_{(P.\ obliquiloculata\ -\ G.\ ruber\ \text{s.l.})}$ estimates suggest more or less comparable upper surface water conditions in the southern SCS during these two periods (Figure 4). This assumption contrasts the notion of *Tian et al.* [2005] for a glacial increase in the depth of the mixed layer due to stronger winter monsoon winds.

[28] 2. Unlike the $\Delta\delta^{18}O$ records, the $\Delta T_{(G.\ ruber\ -\ P.\ obliquiloculata)}$ and $\Delta T_{(\text{Alkenones}\ -\ P.\ obliquiloculata)}$ reconstructions reveal a smaller (~4°C) thermal gradient between surface and subsurface waters during the LGM compared to the late Holocene (~6°C). This suggests a stronger vertical mixing during the LGM compared to the late Holocene (Figure 5). Furthermore, higher $\Delta\delta^{18}O$ values occurred between 11 and 8 ka, indicative of a shallow mixed layer. In contrast, largest differences in ΔT occurred between 6.5 ka and 2.5 ka, indicating less vertical mixing compared to the late Holocene (after 2.5 ka). Our ΔT data support the assertion of a deeper mixed layer during the last glacial (Figures 5c and 5e) in accordance with previous studies [*Tian et al.*, 2005; *Xu*, 2004]. The $\Delta\delta^{18}O$ values, however, do not support the assumption for a deeper mixed layer during the last glacial. What could be the reason for the discrepancy between these approaches?

[29] The largest $\Delta\delta^{18}O$ values indicative of less vertical mixing are recorded between ~11 ka and 8 ka (Figures 4b and 4c). The period between 11 ka and 5 ka, the so-called "Holocene optimum," is arguably characterized by stronger summer monsoon rains in Asia as inferred from model and proxy data [e.g., *Kutzbach*, 1981; *An et al.*, 2000; *He et al.*, 2004; *An et al.*, 2006] and is associated with higher river runoff and fresher sea surface water conditions [*Sirocko et al.*, 1993; *Overpeck et al.*, 1996; *Wang et al.*, 1999]. Paleoecological investigations in the NE Cambodia also indicate that summer monsoon intensity increased during the early Holocene [*Maxwell*, 2001].

[30] Estimates of sea surface salinity ($\delta^{18}O_{seawater}$) at our site reveal that the southern SCS surface water might have been significantly fresher during the early Holocene and Preboreal transition (~11−8 ka) than during the late Holocene [*Steinke et al.*, 2006] (Figure 4d). In this context, we suggest that local changes in salinity may have had a strong influence on the shell $\delta^{18}O$ of the upper mixed layer dwelling species *G. ruber*. Lighter values due to freshwater supply would enhance the $\Delta\delta^{18}O$ toward larger differences and consequently, lead to the interpretation of a weaker mixing. The overriding control of salinity changes on the shell $\delta^{18}O$ of the surface-dwelling species *G. ruber* is further supported by the $\Delta\delta^{18}O_{(P.\ obliquiloculata\ -\ G.\ ruber\ \text{s.l.})}$ and $\Delta\delta^{18}O_{(N.\ dutertrei\ -\ G.\ ruber\ \text{s.l.})}$ estimates (Figures 4b and 4c). As *G. ruber* s.l. has a deeper habitat than *G. ruber* s.s. [*Wang*, 2000; *Kuroyanagi and Kawahata*, 2004; *Kawahata*, 2005; *Steinke et al.*, 2005], the $\delta^{18}O$ of *G. ruber* s.l. is less affected by large variations in salinity caused by varying EAM intensity. Accordingly, $\Delta\delta^{18}O$ values between ~11 ka and 8 ka are less pronounced in the $\Delta\delta^{18}O_{(P.\ obliquiloculata\ -\ G.\ ruber\ \text{s.l.})}$ and $\Delta\delta^{18}O_{(N.\ dutertrei\ -\ G.\ ruber\ \text{s.l.})}$ records (Figures 4b and 4c).

[31] The influence of freshwater on the $\Delta\delta^{18}O$ estimates may also explain the higher glacial $\Delta\delta^{18}O_{(P.\ obliquiloculata\ -\ G.\ ruber\ \text{s.s.})}$ and similar $\Delta\delta^{18}O_{(P.\ obliquiloculata\ -\ G.\ ruber\ \text{s.l.})}$ estimates when compared to the late Holocene (this study) and to core top samples [*Tian et al.*, 2005]. SSS estimates from the same site [*Steinke et al.*, 2006] (Figure 4d) and other southern SCS sites [*Kuhnt et al.*, 2004] indeed show that the southern SCS has been significantly fresher during the LGM. This is interpreted to reflect a higher freshwater contribution due to a closer proximity of the core site to the mouths of the rivers that drained the exposed Sunda Shelf during glacial sea level low stand [*Steinke et al.*, 2006]. In addition, *Sun et al.* [2000] suggested that more precipitation in the southern SCS region was provided by the strengthening EAWM that absorbed moisture when crossing the SCS. This is also indicated by palynological studies, which revealed the occurrence of lowland rain forest on the exposed Sunda Shelf during the last glacial [*Sun et al.*, 2000]. In comparison to our $\Delta\delta^{18}O$ estimates, lower $\Delta\delta^{18}O$ values at the more "open ocean" ODP site 1143 during glacial intervals may reflect the greater distance to the former coastline and consequently, a weaker influence of river runoff/discharge. Given the potential overriding con-

Figure 5. Comparison of different proxy records of the upper water column structure at core site MD01-2390 since the LGM: (a) Mg/Ca SST data of *G. ruber* sensu stricto (s.s.) (red [*Steinke et al.*, 2008]) and *G. ruber* sensu lato (s.l.) (blue [*Steinke et al.*, 2008]) and alkenone SST data (black [*Steinke et al.*, 2008]) (this study); (b) Mg/Ca-based temperature record of *P. obliquiloculata*; (c) thermal gradient between surface and thermocline waters, $\Delta T_{(P.\ obliquiloculata\ -\ G.\ ruber\ \text{s.s.})}$ (black) and $\Delta T_{(P.\ obliquiloculata\ -\ G.\ ruber\ \text{s.l.})}$ (blue); (d) $\Delta T_{(\text{Alkenone-T}\ -\ \text{Mg/Ca-T}\ P.\ obliquiloculata)}$; and (e) $\Delta\delta^{18}O_{(P.\ obliquiloculata\ -\ G.\ ruber\ \text{s.s.})}$ (black) and $\Delta\delta^{18}O_{(P.\ obliquiloculata\ -\ G.\ ruber\ \text{s.l.})}$ (blue). Shaded bars as in Figure 4. The arrows in Figure 5a indicate the modern summer and winter upper water temperatures.

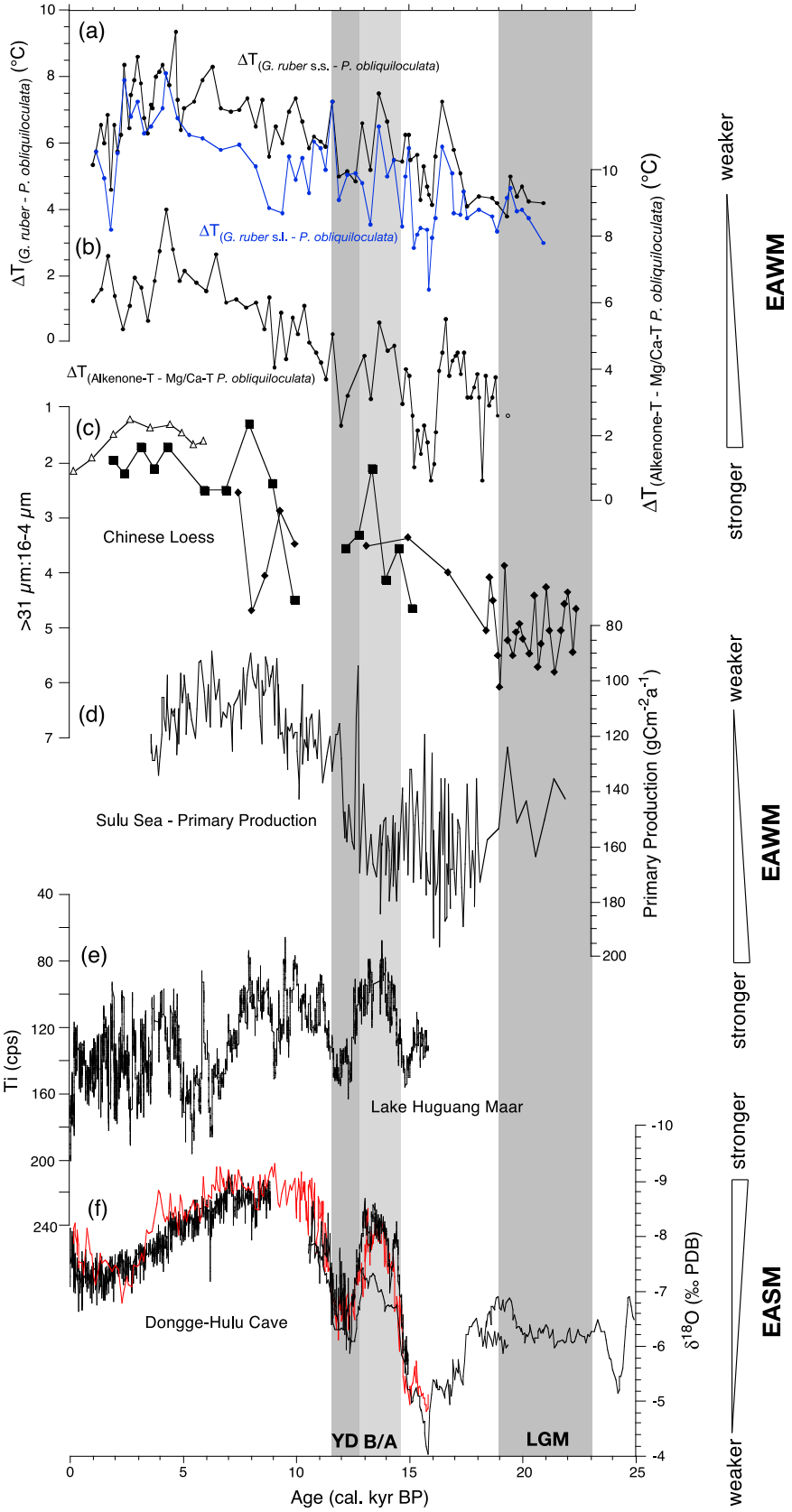
(a)
ΔT(G. ruber s.s. - P. obliquiloculata)
(b)
ΔT(G. ruber s.l. - P. obliquiloculata)
ΔT(Alkenone-T - Mg/Ca-T P. obliquiloculata) (°C)
ΔT(G. ruber - P. obliquiloculata) (°C)
ΔT(Alkenone-T - Mg/Ca-T P. obliquiloculata) (°C)
weaker
stronger
EAWM
(c)
Chinese Loess
>31 μm:16-4 μm
(d)
Sulu Sea - Primary Production
Primary Production (gCm-2a-1)
weaker
stronger
EAWM
(e)
Lake Huguang Maar
Ti (cps)
(f)
Dongge-Hulu Cave
δ18O (‰ PDB)
stronger
weaker
EASM
YD B/A
LGM
Age (cal. kyr BP)

Figure 6

trol of salinity on the $\Delta\delta^{18}O$ estimates, it is doubtful that the $\Delta\delta^{18}O$ values display a true upper ocean thermal gradient. Therefore, the $\Delta\delta^{18}O$ between subsurface and surface dwelling planktonic foraminifera species is not a reliable method to assess changes in the surface water column structure in the southern SCS since the LGM.

6.2. Implications for the EAWM Development Since the LGM

[32] Assuming ΔT reconstructions to be a more reliable approach to assess changes in the surface water column structure, lower $\Delta T_{(G.\ ruber\ -\ P.obliquiloculata)}$ and $\Delta T_{(Alkenones\ -\ P.\ obliquiloculata)}$ values during the late glacial are interpreted to reflect a stronger mixing of the southern SCS surface water column (Figures 6a and 6b), most likely due to a strengthening of EAWM winds. Our results from the southern SCS are in good agreement with a stronger EAWM during the last glacial period inferred from northern SCS records [*Huang et al.*, 1997; *Chen and Huang*, 1998; *Wang et al.*, 1999]. Likewise, results from the Sulu Sea suggest enhanced primary productivity during the last glacial due to a stronger EAWM [*de Garidel-Thoron et al.*, 2001] (Figure 6). $\Delta T_{(G.\ ruber\ -\ P.\ obliquiloculata)}$ and $\Delta T_{(Alkenones\ -\ P.\ obliquiloculata)}$ values were lowest between 16.5 ka and 14.7 ka (Figure 6), during the weakest period of EASM over the last 25 ka in SE Asia as inferred from stalagmite $\delta^{18}O$ records in Hulu and Dongge caves, eastern China (EASM proxy [e.g., *Wang et al.*, 2001, 2008; *Y. Wang et al.*, 2005]). Increased surface water mixing during this period is coeval with the Heinrich 1 period in the North Atlantic region [*Hemming*, 2004]. Model experiments revealed stronger monsoon-overlying westerly winds during Heinrich events that are most likely responsible for the stronger surface water mixing in the southern SCS [*Jin et al.*, 2007].

[33] Starting at ~15 ka, $\Delta T_{(Alkenones\ -\ P.\ obliquiloculata)}$ and $\Delta T_{(G.\ ruber\ -\ P.\ obliquiloculata)}$ gradually increased toward the late Holocene suggesting a shoaling mixed layer and thus, a weakening of the EAWM winds toward the late Holocene. The reconstructed mixed layer depth variations coincide with EAWM changes as recorded in Chinese loess (Figure 6c) [*Stevens et al.*, 2007] and indicate that over the last 21 ka, the EAWM was weakest between 6.5 and 2.5 ka (Figures 6a and 6b). Furthermore, our ΔT data suggest that the YD is also associated with a deeper mixed layer, possibly due to stronger EAWM winds (Figure 5). Evidence for stronger (weaker) winter monsoon winds during the YD (B/A) is further provided by the titanium content of the Lake Huguang Maar sediments in southeast China [*Yancheva et al.*, 2007] (Figure 6e). The Ti content is interpreted as a measure of changes in the aeolian supply of lithogenic material due to varying strength of the winter monsoon winds [*Yancheva et al.*, 2007]. Our reconstructed periods of stronger EAWM between 16.5 ka and 14.7 ka and the YD coincide with higher Lake Huguang Maar Ti contents, which indicate an enhanced aeolian input and thus stronger EAWM winds. Weaker mixing during the B/A and the early Holocene correlates with lower Ti contents, implying a weaker EAWM (Figure 6).

[34] Comparison of our EAWM proxy data with cave stalagmite records [e.g., *Wang et al.*, 2001] (Figure 6f) suggests an inverse behavior of the EAWM and EASM during the last glacial and deglaciation (Figure 6). Periods of stronger surface mixing (e.g., YD) and hence, EAWM strengthening, coincide with higher $\delta^{18}O$ of stalagmites from the Hulu and Dongge caves, which indicates lower summer precipitation rates and thus a weaker EASM (Figure 6). *Yancheva et al.* [2007] also proposed this anticorrelation between the EAWM and EASM, although their proxy interpretation has been questioned recently [*Zhou et al.*, 2009]. Thus, the alternating prevalence of EAWM and EASM most likely represents a common pattern of EAM behavior during the late glacial and deglaciation.

[35] The winter/summer monsoon anticorrelation is not evident during the middle to late Holocene (Figure 6). Instead, it appears that a weaker EAWM during the middle to late Holocene covaried with a weaker EASM. Likewise, the Ti record of *Yancheva et al.* [2007] also lacks a clear winter/summer monsoon anticorrelation during the middle to late Holocene, suggesting that the winter/summer monsoon anticorrelation is not valid for the Holocene period. It appears that the phase relationship between the EASM and EASW systems has changed due to changing glacial to Holocene boundary conditions. However, EAWM proxy records are still sparse to fully support our assertion about the EAWM development since the last LGM, in particular during the middle to late Holocene. In summary, more high-resolution EAWM records are required to confirm our suggestions and to obtain a fundamental understanding of the EAM dynamics.

7. Conclusions

[36] The upper water column structure at site MD01-2390 in the southern SCS during the last 21 ka has been reconstructed using $\delta^{18}O$ and Mg/Ca ratios of surface and subsurface dwelling foraminifera, and alkenone paleothermometry. Based on these results, the following conclusions can be drawn:

[37] The $\Delta\delta^{18}O$ between surface and subsurface dwelling planktonic foraminifera is considerably influenced by changes in local surface water salinities in the southern SCS since the LGM. Due to the potential overriding control of local salinity changes on the $\Delta\delta^{18}O$ estimates, we suggest that $\Delta\delta^{18}O$ values do not display a true upper ocean thermal gradient in the southern SCS.

Figure 6. Comparison of the EAWM proxy records in core MD01-2390 with other climate records. (a) Thermal gradient between surface and thermocline waters, $\Delta T_{(P.\ obliquiloculata\ -\ G.\ ruber\ s.s.)}$ (black) and $\Delta T_{(P.\ obliquiloculata\ -\ G.\ ruber\ s.l.)}$ (blue); (b) $\Delta T_{(Alkenone\text{-}T\ -\ Mg/Ca\text{-}T\ P.\ obliquiloculata)}$; (c) Chinese loess grain size records [*Stevens et al.*, 2007]; (d) Sulu Sea primary productivity [*de Garidel-Thoron et al.*, 2001]; (e) Lake Huguang Maar Ti (cps) record [*Yancheva et al.*, 2007]; and (f) stalagmite $\delta^{18}O$ records from Dongge and Hulu caves [*Wang et al.*, 2001, 2008; *Y. Wang et al.*, 2005]. Shaded bars as in Figure 4.

[38] The ΔT reconstructions using alkenone SSTs, and *G. ruber* and *P. obliquiloculata* Mg/Ca temperatures reveal a smaller thermal gradient between surface and subsurface waters during the LGM compared to the late Holocene. This indicates increased surface water mixing due to enhanced EAWM winds during the LGM. Starting at ~15 ka, the ΔT results suggest a shoaling mixed layer and thus, weakening EAWM winds toward the late Holocene. Largest ΔT between surface and thermocline waters occurred between 6.5 ka and 2.5 ka, indicating less vertical mixing during this period.

[39] Comparison of our EAWM proxy data with cave stalagmite records (EASM proxy) suggest an inverse behavior of the EAWM and EASM during the last glacial and deglaciation. On the other hand, the winter/summer monsoon anticorrelation is not evident during the middle to late Holocene, when a weak EAWM corresponds to a weak EASM.

[40] **Acknowledgments.** We thank the IMAGES program for allowing access to core MD01-2390. This study has been funded by the National Science Council Taiwan through grants to M.-T.C. This study was completed with support from the DFG Research Center/Excellence Cluster "The Ocean in the Earth System," University of Bremen, and the Tongji University, Shanghai, through a fellowship to S.S. J.G. thanks MARUM for financial support via an MARUM fellowship. We express our gratitude to Monika Segl and Helmut Erlenkeuser and their teams for stable isotope analyses. Comments from Gerald Dickens and three anonymous reviewers greatly improved the manuscript.

References

An, C.-B., Z.-D. Feng, and L. Barton (2006), Dry or humid? Mid-Holocene humidity changes in arid and semi-arid China, *Quat. Sci. Rev.*, *25*, 351–361, doi:10.1016/j.quascirev.2005.03.013.

An, Z., S. C. Porter, J. E. Kutzbach, X. Wu, S. Wang, X. Liu, X. Li, and W. Zhou (2000), Asynchronous Holocene optimum of the East Asian monsoon, *Quat. Sci. Rev.*, *19*, 743–762, doi:10.1016/S0277-3791(99)00031-1.

Anand, P., H. Elderfield, and M. H. Conte (2003), Calibration of Mg/Ca thermometry in planktonic foraminifera from a sediment trap time series, *Paleoceanography*, *18*(2), 1050, doi:10.1029/2002PA000846.

Antonov, J. I., R. A. Locarnini, T. P. Boyer, A. V. Mishonov, and H. E. Garcia (2006), *World Ocean Atlas 2005*, vol. 2, *Salinity*, *NOAA Atlas NESDIS*, vol. 62, edited by S. Levitus, 182 pp., NOAA, Silver Spring, Md.

Barker, S., M. Greaves, and H. Elderfield (2003), A study of cleaning procedures used for foraminiferal Mg/Ca paleothermometry, *Geochem. Geophys. Geosyst.*, *4*(9), 8407, doi:10.1029/2003GC000559.

Bemis, B. E., H. J. Spero, J. Bijma, and D. W. Lea (1998), Reevaluation of the oxygen isotopic composition of planktonic foraminifera: Experimental results and revised paleotemperature equations, *Paleoceanography*, *13*, 150–160, doi:10.1029/98PA00070.

Chen, M.-T., and C.-Y. Huang (1998), Ice-volume forcing of the winter monsoon climate in the South China Sea, *Paleoceanography*, *13*, 622–633, doi:10.1029/98PA02356.

Chen, M.-T., C.-C. Huang, U. Pflaumann, C. Waelbroeck, and M. Kucera (2005), Estimating glacial western Pacific sea-surface temperature: Methodological overview and data compilation of surface sediment planktic foraminifer faunas, *Quat. Sci. Rev.*, *24*, 1049–1062, doi:10.1016/j.quascirev.2004.07.013.

Chen, Y.-L., H.-Y. Chen, and C.-W. Chung (2007), Seasonal variability of coccolithophore abundance and assemblage in the northern South China Sea, *Deep Sea Res., Part II*, *54*, 1617–1633, doi:10.1016/j.dsr2.2007.05.005.

Cléroux, C., E. Cortijo, J.-C. Duplessy, and R. Zahn (2007), Deep-dwelling foraminifera as thermocline temperature recorders, *Geochem. Geophys. Geosyst.*, *8*, Q04N11, doi:10.1029/2006GC001474.

Conte, M. H., M.-A. Sicre, C. Rühlemann, J. C. Weber, S. Schulte, D. Schulz-Bull, and T. Blanz (2006), Global temperature calibration of the alkenone unsaturation index ($U^{K'}_{37}$) in surface waters and comparison with surface sediments, *Geochem. Geophys. Geosyst.*, *7*, Q02005, doi:10.1029/2005GC001054.

Curry, W. B., R. C. Thunell, and S. Honjo (1983), Seasonal changes in the isotopic composition of planktonic foraminifera collected in Panama Basin sediment traps, *Earth Planet. Sci. Lett.*, *64*, 33–43, doi:10.1016/0012-821X(83)90050-X.

de Garidel-Thoron, T., L. Beaufort, B. K. Linsley, and S. Dannenmann (2001), Millennial-scale dynamics of the East Asian winter monsoon during the last 200,000 years, *Paleoceanography*, *16*, 491–502, doi:10.1029/2000PA000557.

Ding, Y. (1994), *Monsoons Over China*, 419 pp., Kluwer Acad., Norwell, Mass.

Elderfield, H., and G. Ganssen (2000), Past temperature and $\delta^{18}O$ of surface ocean waters inferred from foraminiferal Mg/Ca ratios, *Nature*, *405*, 442–445, doi:10.1038/35013033.

Fairbanks, R. G., P. H. Wiebe, and A. W. H. Bé (1980), Vertical distribution and isotopic composition of living planktonic foraminifera in the western North Atlantic, *Science*, *207*, 61–63, doi:10.1126/science.207.4426.61.

Fairbanks, R. G., M. Sverdlove, R. Free, P. H. Wiebe, and A. W. H. Bé (1982), Vertical distribution and isotopic fractionation of living planktonic foraminifera from the Panama Basin, *Nature*, *298*, 841–844, doi:10.1038/298841a0.

Farmer, E. C., A. Kaplan, P. B. de Menocal, and J. Lynch-Stieglitz (2007), Corroborating ecological depth preferences of planktonic foraminifera in the tropical Atlantic with the stable oxygen isotope ratios of core top specimens, *Paleoceanography*, *22*, PA3205, doi:10.1029/2006PA001361.

He, Y., W. H. Theakstone, Z. Zhang, D. Zhang, T. Yao, T. Chen, Y. Shen, and H. Pang (2004), Asynchronous Holocene climatic change across China, *Quat. Res.*, *61*, 52–63, doi:10.1016/j.yqres.2003.08.004.

Hemleben, C., M. Spindler, and O. R. Anderson (1989), *Modern Planktonic Foraminifera*, 363 pp., Springer, New York.

Hemming, S. R. (2004), Heinrich events: Massive late Pleistocene detritus layers of the North Atlantic and their global climate imprint, *Rev. Geophys.*, *42*, RG1005, doi:10.1029/2003RG000128.

Huang, B., Z. Jian, X. Cheng, and P. Wang (2003), Foraminiferal responses to upwelling variations in the South China Sea over the last 220 000 years, *Mar. Micropaleontol.*, *47*, 1–15, doi:10.1016/S0377-8398(02)00045-2.

Huang, C.-Y., S.-F. Wu, M. Zhao, M.-T. Chen, C.-H. Wang, X. Tu, and P. B. Yuan (1997), Surface ocean and monsoon climate variability in the South China Sea since the last glaciation, *Mar. Micropaleontol.*, *32*, 71–94, doi:10.1016/S0377-8398(97)00014-5.

Hughen, K. A., et al. (2004), Marine04 marine radiocarbon age calibration, 0–26 cal kyr BP, *Radiocarbon*, *46*, 1059–1086.

Jian, Z., B. Huang, W. Kuhnt, and H.-L. Lin (2001), Late Quaternary upwelling intensity and East Asian monsoon forcing in the South China Sea, *Quat. Res.*, *55*, 363–370, doi:10.1006/qres.2001.2231.

Jin, L., F. Chen, A. Ganopolski, and M. Claussen (2007), Response of East Asian climate to Dansgaard/Oeschger and Heinrich events in a coupled model of intermediate complexity, *J. Geophys. Res.*, *112*, D06117, doi:10.1029/2006JD007316.

Kawahata, H. (2005), Stable isotopic composition of two morphotypes of *Globigerinoides ruber* (white) in the subtropical gyre in the North Pacific, *Paleontol. Res.*, *9*, 27–35, doi:10.2517/prpsj.9.27.

Kienast, M., S. Steinke, K. Stattegger, and S. E. Calvert (2001), Synchronous tropical South China Sea SST change and Greenland warming during deglaciation, *Science*, *291*, 2132–2134, doi:10.1126/science.1057131.

Kudrass, H. R., A. Hofmann, H. Doose, K. Emeis, and H. Erlenkeuser (2001), Modulation and amplification of climatic changes in the Northern hemisphere by the Indian summer monsoon during the past 80 k.y, *Geology*, *29*, 63–66, doi:10.1130/0091-7613(2001)029<0063:MAAOCC>2.0.CO;2.

Kuhnt, W., A. Holbourn, R. Hall, M. Zuvela, and R. Käse (2004), Neogene history of the Indonesian Throughflow, in *Continent-Ocean Interactions Within East Asian Marginal Seas*, *Geophys. Monogr. Ser.*, vol. 149, edited by P. Clift et al., pp. 299–320, AGU, Washington, D. C.

Kuroyanagi, A., and H. Kawahata (2004), Vertical distribution of living planktonic foraminifera in the seas around Japan, *Mar. Micropaleontol.*, *53*, 173–196, doi:10.1016/j.marmicro.2004.06.001.

Kutzbach, J. E. (1981), Monsoon climate of the early Holocene: Climate experiment with the Earth's orbital parameters for 9000 years ago, *Science*, *214*, 59–61, doi:10.1126/science.214.4516.59.

Lea, D. W., D. K. Pak, and H. J. Spero (2000), Climate impact of Late Quaternary equatorial Pacific sea surface temperature variations, *Science*, *289*, 1719–1724, doi:10.1126/science.289.5485.1719.

Lin, H.-L., and H.-Y. Hsieh (2007), Seasonal variations of modern planktonic foraminifera in the South China Sea, *Deep Sea Res., Part II*, *54*, 1634–1644, doi:10.1016/j.dsr2.2007.05.007.

Lin, H.-L., W.-C. Wang, and G.-W. Hung (2004), Seasonal variation of planktonic foraminiferal isotopic composition from sediment traps in the South China Sea, *Mar. Micropaleontol.*, *53*, 447–460, doi:10.1016/j.marmicro.2004.08.004.

Locarnini, R. A., A. V. Mishonov, J. I. Antonov, T. P. Boyer, and H. E. Garcia (2006), *World Ocean Atlas 2005*, vol. 1, *Temperature*, *NOAA Atlas NESDIS*, vol. 61, edited by S. Levitus, 182 pp., NOAA, Silver Spring, Md.

Löwemark, L., W.-L. Hong, T.-F. Yui, and G.-W. Hung (2005), A test of different factors influencing the isotopic signal of planktonic foraminifers in surface sediments from the northern South China Sea, *Mar. Micropaleontol.*, *55*, 49–62, doi:10.1016/j.marmicro.2005.02.004.

Löwemark, L., I. K. Konstaninou, and S. Steinke (2008), Bias in foraminiferal multispecies reconstructions of paleohydrographic conditions caused by foraminiferal abundance variations and bioturbational mixing: A model approach, *Mar. Geol.*, *256*, 101–106, doi:10.1016/j.margeo.2008.10.005.

Maxwell, A. L. (2001), Holocene monsoon changes inferred from lake sediment pollen and carbonate records, northeastern Cambodia, *Quat. Res.*, *56*, 390–400, doi:10.1006/qres.2001.2271.

Mix, A. C., E. Bard, and R. Schneider (2001), Environmental processes of the ice age: Land, oceans, glaciers (EPILOG), *Quat. Sci. Rev.*, *20*, 627–657, doi:10.1016/S0277-3791(00)00145-1.

Mohtadi, M., S. Steinke, J. Groeneveld, H. G. Fink, T. Rixen, D. Hebbeln, B. Donner, and B. Herunadi (2009), Low-latitude control on seasonal and interannual changes in planktonic foraminiferal flux and shell geochemistry off South Java: A sediment trap study, *Paleoceanography*, *24*, PA1201, doi:10.1029/2008PA001636.

Overpeck, J., D. Anderson, S. Trumdore, and W. Prell (1996), The southwest Indian monsoon over the last 18000 years, *Clim. Dyn.*, *12*, 213–225, doi:10.1007/BF00211619.

Paillard, D., L. Labeyrie, and P. Yiou (1996), Macintosh program performs time-series analysis, *Eos Trans. AGU*, *77*(39), 379, doi:10.1029/96EO00259.

Pelejero, C., and J. O. Grimalt (1997), The correlation between the U^{k}_{37} index and sea surface temperatures in the warm boundary: The South China Sea, *Geochim. Cosmochim. Acta*, *61*, 4789–4797, doi:10.1016/S0016-7037(97)00280-9.

Pelejero, C., J. O. Grimalt, S. Heilig, M. Kienast, and L. Wang (1999), High-resolution U^{K}_{37} temperature reconstructions in the South China Sea over the past 220 kyr, *Paleoceanography*, *14*, 224–231, doi:10.1029/1998PA900015.

Qu, T., Y. Du, J. Gan, and D. Wang (2007), Mean seasonal cycle of isothermal depth in the South China Sea, *J. Geophys. Res.*, *112*, C02020, doi:10.1029/2006JC003583.

Rashid, H., B. P. Flower, R. Z. Poore, and T. M. Quinn (2007), A ~25 ka Indian Ocean monsoon variability record from the Andaman Sea, *Quat. Sci. Rev.*, *26*, 2586–2597, doi:10.1016/j.quascirev.2007.07.002.

Ravelo, A. C., and D. H. Andreasen (1999), Using planktonic foraminifera as monitors of the tropical surface ocean, in *Reconstructing Ocean History: A Window Into the Future*, edited by F. Abrantes and A. C. Mix, pp. 217–244, Plenum, New York.

Ravelo, A. C., and R. G. Fairbanks (1992), Oxygen isotopic composition of multiple species of planktonic foraminifera: Recorders of the modern photic zone temperature gradient, *Paleoceanography*, *7*, 815–831, doi:10.1029/92PA02092.

Ravelo, A. C., and N. J. Shackleton (1995), Evidence for surface-water circulation changes at Site 851 in the eastern tropical Pacific Ocean, *Proc. Ocean Drill. Program Sci. Results*, *138*, 503–514.

Shaw, P.-T., and S.-Y. Chao (1994), Surface circulation in the South China Sea, *Deep Sea Res., Part I*, *41*, 1663–1683, doi:10.1016/0967-0637(94)90067-1.

Sirocko, F., M. Sarnthein, H. Erlenkeuser, H. Lange, M. Arnold, and J. C. Duplessy (1993), Century-scale events in monsoonal climate over the past 24,000 years, *Nature*, *364*, 322–324, doi:10.1038/364322a0.

Steinke, S., M. Kienast, U. Pflaumann, M. Weinelt, and K. Stattegger (2001), A high-resolution sea-surface temperature record from the tropical South China Sea (16,500–3000 yr B.P.), *Quat. Res.*, *55*, 352–362, doi:10.1006/qres.2001.2235.

Steinke, S., H.-Y. Chiu, P.-S. Yu, C.-C. Shen, L. Löwemark, H.-S. Mii, and M.-T. Chen (2005), Mg/Ca ratios of two *Globigerinoides ruber* (white) morphotypes: Implications for reconstructing past tropical/subtropical surface water conditions, *Geochem. Geophys. Geosyst.*, *6*, Q11005, doi:10.1029/2005GC000926.

Steinke, S., H.-I. Chiu, P.-S. Yu, C.-C. Shen, H. Erlenkeuser, L. Löwemark, and M.-T. Chen (2006), On the influence of sea level and monsoon climate on the southern South China Sea freshwater budget over the last 22,000 years, *Quat. Sci. Rev.*, *25*, 1475–1488, doi:10.1016/j.quascirev.2005.12.008.

Steinke, S., M. Kienast, J. Groeneveld, L.-C. Lin, M.-T. Chen, and R. Rendle-Bühring (2008), Proxy dependence of the temporal patterns of deglacial warming in the tropical South China Sea: Toward resolving seasonality, *Quat. Sci. Rev.*, *27*, 688–700, doi:10.1016/j.quascirev.2007.12.003.

Stephens, M., D. Mattey, D. D. Gilbertson, and C. V. Murray-Wallace (2008), Shell-gathering from mangroves and the seasonality of the Southeast Asian monsoon using high-resolution stable isotopic analysis of the tropical estuarine bivalve (*Geloina ersosa*) from the Great Cave of Niah, Sarawak: Methods and reconnaissance of molluscs of early Holocene and modern times, *J. Archaeol. Sci.*, *35*, 2686–2697, doi:10.1016/j.jas.2008.04.025.

Stevens, T., D. S. G. Thomas, S. J. Armitage, H. R. Lunn, and H. Lu (2007), Reinterpreting climate proxy records from Late Quaternary Chinese loess: A detailed OSL investigation, *Earth Sci. Rev.*, *80*, 111–136, doi:10.1016/j.earscirev.2006.09.001.

Stuiver, M., P. M. Grootes, and T. F. Braziunas (1995), The GISP2 δ^{18}O climate record of the past 16,500 years and the role of the Sun, ocean, and volcanoes, *Quat. Res.*, *44*, 341–354, doi:10.1006/qres.1995.1079.

Stuiver, M., P. J. Reimer, E. Bard, J. W. Beck, G. S. Burr, K. A. Hughen, B. Kromer, G. McCormac, J. Van der Pflicht, and M. Spurk (1998), INTCAL98 radiocarbon age calibration, 24,000–0 cal BP, *Radiocarbon*, *40*, 1041–1083.

Sun, X., X. Li, and X. Chen (2000), The vegetation and climate at the last glaciation on the emerged continental shelf of the South China Sea, *Palaeogeogr. Palaeoclimatol. Palaeoecol.*, *160*, 301–316, doi:10.1016/S0031-0182(00)00078-X.

Tamburini, F., T. Adatte, K. Föllmi, S. M. Bernasconi, and P. Steinmann (2003), Investigating the history of East Asian monsoon and climate during the last glacial-interglacial period (0–140 000 years): Mineralogy and geochemistry of ODP Sites 1143 and 1144, South China Sea, *Mar. Geol.*, *201*, 147–168, doi:10.1016/S0025-3227(03)00214-7.

Tian, J., P. Wang, R. Chen, and X. Cheng (2005), Quaternary upper ocean thermal gradient variations in the South China Sea: Implications for East Asian monsoon climate, *Paleoceanography*, *20*, PA4007, doi:10.1029/2004PA001115.

Waelbroeck, C., L. Labeyrie, E. Michel, J. C. Duplessy, J. F. McManus, K. Lambeck, E. Balbon, and M. Labracherie (2002), Sea-level and deep water temperature changes derived from benthic foraminifera isotopic record, *Quat. Sci. Rev.*, *21*, 295–305, doi:10.1016/S0277-3791(01)00101-9.

Wang, L. (2000), Isotopic signals in two morphotypes of *Globigerinoides ruber* (white) from the South China Sea: Implications for monsoon climate change during the last glacial cycle, *Palaeogeogr. Palaeoclimatol. Palaeoecol.*, *161*, 381–394, doi:10.1016/S0031-0182(00)00094-8.

Wang, L., M. Sarnthein, H. Erlenkeuser, J. Grimalt, P. Grootes, S. Heilig, E. Ivanova, M. Kienast, C. Pelejero, and U. Pflaumann (1999), East Asian monsoon climate during the late Pleistocene: High-resolution sediment records from the South China Sea, *Mar. Geol.*, *156*, 245–284, doi:10.1016/S0025-3227(98)00182-0.

Wang, P., S. Clemens, L. Beaufort, P. Braconnot, G. Ganssen, Z. Jian, P. Kershaw, and M. Sarnthein (2005), Evolution and variability of the Asian monsoon system: State of the art and outstanding issues, *Quat. Sci. Rev.*, *24*, 595–629, doi:10.1016/j.quascirev.2004.10.002.

Wang, Y. J., H. Cheng, R. L. Edwards, Z. S. An, J. Y. Wu, C.-C. Shen, and J. A. Dorale (2001), A high-resolution absolute-dated late Pleistocene monsoon record from Hulu Cave, China, *Science*, *294*, 2345–2348, doi:10.1126/science.1064618.

Wang, Y., H. Cheng, R. L. Edwards, Y. He, X. Kong, Z. An, J. Wu, M. J. Kelly, C. A. Dykoski, and X. Li (2005), The Holocene Asian monsoon: Links to solar changes and North Atlantic climate, *Science*, *308*, 854–857, doi:10.1126/science.1106296.

Wang, Y., H. Cheng, R. L. Edwards, X. Kong, X. Shao, S. Chen, J. Wu, X. Jiang, X. Wang, and Z. An (2008), Millennial- and orbital-scale changes in the East Asian monsoon over the past 224,000 years, *Nature*, *451*, 1090–1093, doi:10.1038/nature06692.

Wiesner, M. G., L. Zheng, H. K. Wong, Y. Wang, and W. Chen (1996), Fluxes of particulate matter in the South China Sea, in *Particle Flux in the Ocean*, *SCOPE Ser.*, vol. 57, edited by

V. Ittekkot et al., pp. 293–312, John Wiley, Chichester, U. K.

Wyrtki, K. (1961), *Physical oceanography of the Southeast Asian waters*, NAGA report, Scripps Inst. of Oceanogr., Univ. of Calif., La Jolla.

Xu, J. (2004), Quaternary planktonic foraminiferal assemblages in the southern South China Sea and paleoclimatic variations, Ph.D. thesis, 98 pp., Tongji Univ., Shanghai, China.

Xu, J., P. Wang, B. Huang, Q. Li, and Z. Jian (2005), Response of planktonic foraminifera to glacial cycles: Mid-Pleistocene change in the southern South China Sea, *Mar. Micropaleontol.*, *54*, 89–105.

Yancheva, G., N. R. Nowacyzk, J. Mingram, P. Dulski, G. Schettler, J. F. W. Negendank, J. Liu, D. M. Sigman, L. C. Peterson, and G. H. Haug (2007), Influence of the intertropical convergence zone on the East Asian monsoon, *Nature*, *445*, 74–77, doi:10.1038/nature05431.

Yu, P.-S., C.-C. Huang, Y. Chin, H.-S. Mii, and M.-T. Chen (2006), Late Quaternary East Asian monsoon variability in the South China Sea: Evidence from planktonic foraminifera faunal and hydrographic gradient records, *Palaeogeogr. Palaeoclimatol. Palaeoecol.*, *236*, 74–90, doi:10.1016/j.palaeo.2005.11.038.

Zhao, M., C.-Y. Huang, C.-C. Wang, and G. Wie (2006), A millennial-scale $U^{K'}_{37}$ sea-surface temperature record from the South China Sea (8°N) over the last 150 kyr: Monsoon and sea-level influence, *Palaeogeogr. Palaeoclimatol. Palaeoecol.*, *236*, 39–55, doi:10.1016/j.palaeo.2005.11.033.

Zhou, H., B.-S. Wang, H. Guan, Y.-J. Lai, C.-F. You, J. Wang, and H.-J. Yang (2009), Constraints from strontium and neodymium isotopic ratios and trace elements on the sources of the sediments in Lake Huguang Maar, *Quat. Res.*, *72*, 289–300, doi:10.1016/j.yqres.2009.06.005.

M.-T. Chen and L.-C. Lin, Institute of Applied Geosciences, National Taiwan Ocean University, Keelung 20224, Taiwan.

J. Groeneveld, Alfred-Wegener-Institut für Polar- und Meeresforschung, D-27515 Bremerhaven, Germany.

L. Löwemark, Department of Geology and Geochemistry, Stockholm University, SE-106 91 Stockholm, Sweden.

M. Mohtadi, R. Rendle-Bühring, and S. Steinke, MARUM-Zentrum für Marine Umweltwissenschaften, University of Bremen, D-28334 Bremen, Germany. (ssteinke@uni-bremen.de)